Hybrid Redox Chemistry in Defective Titanium Polyanion Nanobelt Cathodes for Advanced Magnesium−Ion Batteries

Jianbiao Wang, §[a] Xian Yi Tan, §[a,b] Man-Fai Ng, §[c] Gang Wu, §[c] Gaoliang Yang, [a] Tanmay Ghosh, [a] Carina Yi Jing Lim, [d] Wutthikrai Busayaporn, [e] Wanwisa Limphirat,[e] Dechmongkhon Kaewsuwan,[e] Deviprasath Chinnadurai,[a] Zhenxiang Xing,[a] Hongfei Liu, [a] Yi Ren, [a] Qingyu Yan, *[b] Zhi Wei Seh*[a]

[a] Dr. J. Wang, Dr. X. Y. Tan, Dr. G. Yang, Dr. T. Ghosh, Dr. D. Chinnadurai, Z. Xing, Dr. H. Liu, Dr. Y. Ren, Prof. Z. W. Seh
Institute of Materials Research and Engineering (IMRE), Agency for Science, Technology and Research (A*STAR), 2 Fusionopolis Way, Innovis #08-03, Singapore 138634, Republic of Singapore
E-mail: sehzw@imre.a-star.edu.sg
§These authors contributed equally to this work

[b] Dr. X. Y. Tan, Prof. Q. Yan
School of Materials Science and Engineering, Nanyang Technological University, 50 Nanyang Avenue, Singapore 639798, Republic of Singapore
E-mail: alexyan@ntu.edu.sg

[c] Dr. M.-F. Ng, Dr. G. Wu
Institute of High Performance Computing (IHPC), Agency for Science, Technology and Research (A*STAR), 1 Fusionopolis Way, #16-16 Connexis, Singapore 138632, Republic of Singapore

[d] C. Y. J. Lim
Department of Materials Science and Engineering, Stanford University, Stanford, CA, 94305, USA

[e] Dr. W. Busayaporn, Dr. W. Limphirat, Dr. D. Kaewsuwan
Synchrotron Light Research Institute, 111 Moo 6 University Avenue, Muang, Nakhon Ratchasima 30000, Thailand.

Supporting information for this article is given via a link at the end of the document.

Abstract: Parasitic reactions have hampered transition metal chalcogenide cathodes in magnesium−ion batteries (MIBs), especially for conversion−type cathodes. To fully harness its high theoretical capacity and restrict undesirable side reactions, a defective titanium polyanion cathode (V_s−TiS_3) with exposed (001) facets was prepared via a fast−quenching treatment. The performance of the cathode material was investigated in MIBs for the first time, demonstrating a new hybrid energy storage mechanism involving both insertion and conversion reactions. Moreover, the defective TiS_2 formed during cycling was found to have a strong adsorption effect on the side products of magnesium polysulfides (MgS_x), boosting magnesium storage performance. Consequently, the electrodes delivered a substantial capacity of 717.3 mAh g^{-1} at 25 mA g^{-1}, and a high capacity of 291.5 mAh g^{-1} at 500 mA g^{-1} after 100 cycles, surpassing the performance of previously reported MIBs at the same density. When employed in pouch cells, a high energy density of 220 Wh kg^{-1} was achieved. Lastly, this cathode material was also adapted for other mono/multivalent metal−ion batteries (e.g., Li^+, Na^+, Al^{3+}), demonstrating its versatility.

Introduction

Monovalent−ion batteries have been intensively studied in the last few decades.[1] However, their limited energy density and safety issues have sparked increased interest in multivalent−ion batteries, owing to the greater natural abundance, lower cost, and higher safety associated with multivalent metals.[2] Magnesium−ion batteries (MIBs) have been attracting great interest for use in large−scale energy storage devices, owing to advantages including their high volumetric capacity (3833 mAh cm^{-3}) and low redox potential [−2.37 V *vs.* standard hydrogen electrode (SHE)].[2b, 3] However, their development has been hampered by the paucity of suitable materials as cathodes, due to the strong electrostatic interaction between the high charge density of Mg^{2+} and the lattice of host materials.[4] A myriad of materials have been previously explored as cathodes, including metal oxides, Prussian blue analogues, metal dichalcogenides, and polyanions.[3a, 5]

The high theoretical capacity and low charge density (weak electrostatic interaction) of transition metal chalcogenides (TMCs) poise them as promising candidates for cathodes for MIBs.[6] [7] However, disadvantages including large volumetric changes, low electronic conductivity, as well as unexpected side reactions limit the practical applicability of TMCs in MIBs.[8] Notably, TMC cathodes are plagued by shuttling effects of MgS_x intermediates, especially in conversion-type TMC cathodes, resulting in irreversible capacity loss and poor cycling stability.[9] Fabricating metal sulfide cathodes with high capacities and stability thus remains an elusive goal. To mitigate this, we need to design cathode materials to effectively confine these MgS_x intermediates whilst enabling these intermediates to remain redox active for magnesium storage.

Titanium sulfide (TiS_2) is a representative TMC with a typical insertion mechanism when used as an electrode.[10] Unlike conventional TMCs, two−dimensional TiS_2 has excellent electronic conductivity, which allows for the fast transport of electrons, consequently improving the electrochemical kinetics in

the insertion/extraction of Mg^{2+}.[11] However, the limited insertion sites for TiS_2 restrict their energy density, which may be circumvented by utilizing TMC−based cathodes with chalcogenide−rich anions instead.

Therefore, to strike a balance between the high capacity of chalcogenides and parasitic side reactions in TMCs, we uncovered a hybrid energy storage mechanism involving both conversion and insertion reactions, in defective TiS_3 nanobelt cathode with exposed (001) facets (V_s−TiS_3) for MIBs. It is noteworthy that both the V_s−TiS_3 material as well as its method of preparation (fast quenching treatment to produce S vacancies) are being applied to magnesium batteries for the first time. The hybrid energy storage mechanism and its accompanying phase evolutions are supported by transmission electron microscopy (TEM), X−ray absorption spectroscopy (XAS), cryogenic TEM (cryo−TEM), and time−of−flight secondary ion mass spectrometry (TOF−SIMS). Notably, unlike conventional conversion−type or insertion−type TMC cathodes, the increased presence of sulfur anions in V_s−TiS_3 is postulated to increase capacity via conversion reactions, whilst the following insertion mechanism constrains the shuttle effects and facilitates stable electrochemical processes. Furthermore, the S vacancies in V_s−TiS_3, derived from rapid quenching of TiS_3 nanobelts in ice water, can also improve its electronic conductivity and provide more active sites for the insertion/extraction of Mg^{2+}, based on density functional theory (DFT) calculations. Through crystal engineering, the single−crystal structure, coupled with the exposed (001) facets, is advantageous to the electrode's performance, as validated by machine−learned force field-based molecular dynamics (MLFF-MD) simulations.

Consequently, the optimized cathode V_s−TiS_3 nanobelts demonstrated a reversible capacity of 717.3 mAh g^{-1} at 25 mA g^{-1} after 90 cycles, outperforming other TMC−based electrodes. Besides, when evaluated at the scale of pouch cells, the electrode also maintained good cycling performance with the highest gravimetric energy density of 220 Wh kg^{-1} at 25 mA g^{-1}, indicating great potential for practical applications. Moreover, we also highlight the versatility of this electrode via the evaluation of electrochemical performances in other mono/multivalent metal−ion batteries (e.g., Li^+, Na^+, Al^{3+}). The promising performance, coupled with the investigation into the working mechanisms presented herein may provide some insight into the fabrication of advanced cathodes from the perspective of analogous sulfur−based electrodes.

Results and Discussion

We first used DFT calculations to predict the electrochemical properties of TiS_3, and defective V_s−TiS_3, basing them on the configuration of Mg^{2+} diffusion (Fig. 1A, B). The calculated Mg^{2+} diffusion energy barrier in V_s−TiS_3 (0.28 eV) is lower than that of TiS_3 (0.35 eV), reflecting the enhanced diffusivity of Mg^{2+} in V_s−TiS_3 facilitated by the presence of S vacancies (Fig. 1C, D). The presence of S defects also reduces the bandgap of TiS_3 from 1.14 eV (Fig. S1(A, B)) to 1.03 eV (Fig. 1E, F) in the resulting V_s−TiS_3, enhancing the electronic conductivity and greatly boosting electron transport. Since TiS_3 is rich in S anions, we hypothesize its transition to V_s−TiS_2 during the discharge process (Fig. 1G−I). The binding configurations between TiS_2 and MgS_x (Fig. 1J−N), and likewise between V_s−TiS_2 and MgS_x (Fig. 1O−S), indicate both TiS_2 and V_s−TiS_2 to have an adsorption effect on magnesium polysulfides (MgS_x, x=1, 2, 4, 6, and 8). Interestingly, the calculated adsorption energies for V_s−TiS_2 are lower than those of TiS_2, signifying that defective V_s−TiS_2 is more energetically favorable for anchoring of MgS_x intermediates near the S vacancies, and further highlights the potential of V_s−TiS_3 for use as a cathode material (Table S2).

Based on the favorable DFT calculations, we prepared TiS_3 nanobelts and V_s−TiS_3 nanobelts (Fig. 2A), creating the S vacancies in V_s−TiS_3 nanobelts via the quick quenching process. XRD analyses of TiS_3 and V_s−TiS_3 (Fig. 2B) match, indicating successful preparation of V_s−TiS_3. XPS surveys indicated the presence of Ti and S for both samples (Fig. S2). Deconvoluting the Ti 2p peaks (Fig. 2C) yields peaks at 456.6 eV and 462.6 eV, as well as at 459.4 eV and 465.4 eV, corresponding to the presence of Ti−S and Ti−O, respectively.[12] For TiS_3, peaks of S 2p at 163.4 eV, 162.3 eV, and 161.1 eV are observed as expected, associated with the presence of $(S_2)^{2-}$ and S^{2-}, respectively (Fig. 2D).[13] In contrast, the corresponding binding energies of the S 2p peaks of V_s−TiS_3 are slightly shifted to lower binding energies, as a consequence of the presence of S vacancies.[14] The Raman spectra show four characteristic peaks of TiS_3 (Fig. 2E), namely (1) 175.3 cm^{-1} corresponding to rigid chain vibrations; (2) 299.1 cm^{-1} and 368.8 cm^{-1} involving internal vibrations within each layer; and (3) 556.5 cm^{-1} corresponding to nonbridging S–S pair vibrations.[15] Since the upshift of the band is from the mode of S–S diatomic motions in TiS_3, it further supports the presence of S vacancies in V_s−TiS_3.[16]

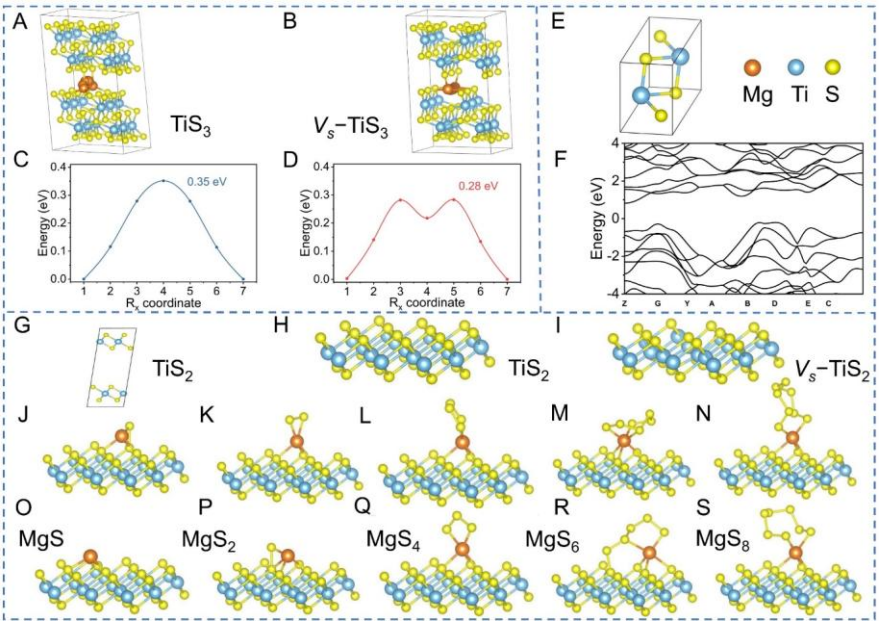

Fig. 1 DFT calculations: Configuration of Mg^{2+} diffusion in (A) TiS_3, (B) V_s−TiS_3. The corresponding Mg^{2+} diffusion energy barriers in (C) TiS_3, and (D) V_s−TiS_3. (E) Configuration, and (F) corresponding band structure of V_s−TiS_3. Structures of (G, H) TiS_2, and (I) defective TiS_2 (V_s−TiS_2). Optimized atomic structures of MgS, MgS_2, MgS_4, MgS_6, and MgS_8 cluster adsorbed on facet of (J–N) TiS_2, and (O–S) V_s−TiS_2.

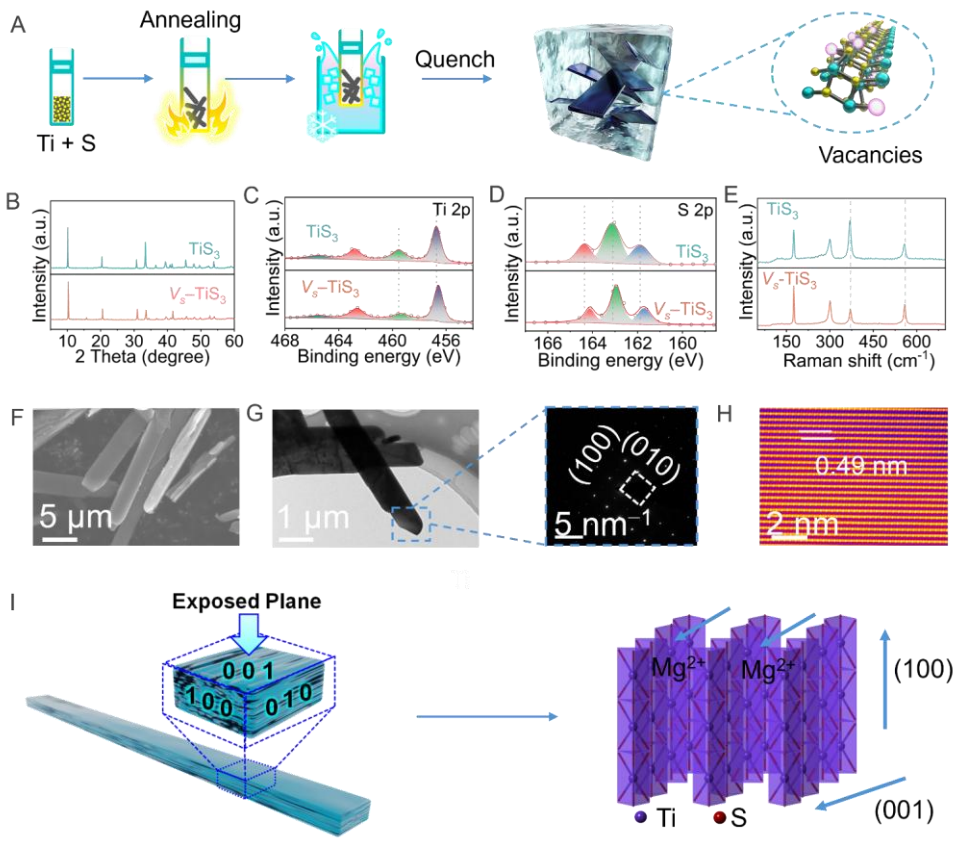

Fig. 2 Material Characterizations: (A) Schematic illustration of the material syntheses, (B) XRD patterns and XPS spectra of (C) Ti 2p, (D) S 2p. (E) Raman spectra of TiS_3 nanobelts, and V_s–TiS_3 nanobelts, respectively. (F) SEM image, (G) TEM image and corresponding SAED pattern), (H) HAADF-STEM image of V_s–TiS_3 nanobelts. (I) Schematic illustration of exposed (001) plane in TiS_3 structure providing multichannel Mg^{2+} transport.

The SEM and TEM images (Fig. 2F, G) reveal V_s–TiS_3 to possess nanobelt morphology. This is consistent with the structure observed for TiS_3 nanobelts (Fig. S3), indicating that the quenching treatment does not affect morphology. Further, the selected area electron diffraction (SAED) pattern of the V_s–TiS_3 nanobelts reflects that the single crystalline characteristic with periodic arrangements of (100) plane and (010) plane (Fig. 2G) is maintained. This allows us to infer that the defective single–crystal V_s–TiS_3 nanobelts have exposed (001) facets. Moreover, High–Angle Annular Dark–Field Scanning Transmission Electron Microscopy (HAADF–STEM) of V_s–TiS_3 nanobelts exhibit the typical lattice fringe of the (100) plane, indicating that the nanobelts grow along the direction of (100) plane (Fig. 2H). Scanning transmission electron microscopy (STEM) of V_s–TiS_3 nanobelts and corresponding elemental maps reveal homogeneous distribution of elemental Ti and S (Fig. S4, S5), supporting the model of growth described above. Likewise, the SAED and HRTEM images of TiS_3 nanobelts display the same exposed facets and single crystalline features observed in V_s–TiS_3 nanobelts (Fig. S6). We posit that such crystalline orientation (Fig. 2I) can provide multiple channels for Mg^{2+} movement and enhance magnesium storage performance.

To evaluate the superiority of V_s–TiS_3 nanobelts as cathodes in MIBs, we performed a series of electrochemical tests (Fig. 3). The cyclic voltammetry (CV) curves at 0.2 mV s^{-1} (Fig. 3A) show

decreasing peak separation between the oxidation and anodic peaks with increasing cycles, demonstrating a gradual enhancement of electrochemical kinetics over initial cycles. The redox peaks at 0.92 V/1.49 V are associated with the conversion reaction from TiS_3 to TiS_2, while another pair of redox peaks (0.75 V/0.91 V) are related to insertion/extraction of Mg^{2+}, in contrast with CV curves and charge/discharge curves of TiS_2 (Fig. S7, S8). Additionally, the overlapping of the CV curves after 25 cycles demonstrates the electrochemical stability of the cathode (Fig. S8B). When cycled at 50 mA g^{-1} (Fig. S9), the cathode demonstrated a high capacity of 703 mAh g^{-1}, exceeding the performance of metal sulfide cathodes reported in previous studies.[3a, 9, 17] Conversely, the TiS_3 nanobelt cathode delivered an inferior capacity of 382 mAh g^{-1}, reflecting the improved cycling performance with the presence of S vacancies. The corresponding charge−discharge profiles illustrate increased capacity from the 10th to 20th cycle, consistent with the trend of cycling performance observed (Fig. S10). At a current density of 25 mA g^{-1}, the cathode achieved a notable capacity of 717.3 mAh g^{-1} after 90 cycles, which exceeds capacities previously reported for TMC−based cathodes in MIBs (Fig. S11, S12).[3a, 9, 17b] At a current density of 100 mA g^{-1}, the cathode of V_s−TiS_3 demonstrates good cycling capacity, maintaining a capacity of 389 mAh g^{-1} after 80 cycles, which is higher than that of TiS_3 with an inferior capacity of 239 mAh g^{-1} (Fig. 3B, Fig. S13). The corresponding charge−discharge profiles after 50th cycles demonstrated prolonged voltage plateaus in contrast with those after 25th cycles, indicating improved electrochemical process (Fig. 3C, Fig. S14). The corresponding Coulombic efficiency exceeding 100% after 30 cycles is attributed to shuttling effects of magnesium polysulfides. At a large current density of 500 mA g^{-1}, the cathode can be cycled over 100 cycles with a capacity of 291.5 mAh g^{-1} (Fig. 3D, S15). The initial cycles with high Coulombic efficiency are due to the cathode activation process at a low current density of 50 mA g^{-1}. For V_s−TiS_3, the capacities of 505.3 mAh g^{-1}, 349.8 mAh g^{-1}, 281.7 mAh g^{-1}, and 211.1 mAh g^{-1} are achieved at current densities of 25 mA g^{-1}, 100 mA g^{-1}, 200 mA g^{-1} and 500 mA g^{-1} respectively, while the electrode of TiS_3 deliver consistently lower capacities of 432.9 mAh g^{-1}, 315.8 mAh g^{-1}, 198.9 mAh g^{-1}, and 103.2 mAh g^{-1} across corresponding current densities (Fig. S16). The intensity of dQ/dV curve after 50th cycle is stronger than that after 25th cycle, indicating enhanced redox electrochemical kinetics (Fig. 3E). To demonstrate its versatility, the optimized V_s−TiS_3 nanobelts were also investigated as electrodes in lithium−ion batteries (LIBs), sodium−ion batteries (SIBs), and aluminum−ion batteries (AIBs). The electrode delivered a stable capacities of 634 mAh g^{-1} after 1000 cycles in LIBs and 305 mAh g^{-1} after 650 cycles at 500 mA g^{-1} in SIBs, outperforming previously reported titanium sulfide−based electrodes for both systems (Fig. S17, S18, S19, and Table S3).[11, 18a, 18b,18c, 18d, 18e] We further utilize the electrodes in AIBs (Fig. S20), validating the flexibility of the cathode chemistry to other metal ion systems. In contrast, the electrode of TiS_3 demonstrates inferior electrochemical storage performances across LIBs, SIBs, and AIBs (Fig. S21−25).

To understand the electrochemical performance of V_s−TiS_3 nanobelts, we obtained electrochemical impedance spectra (EIS) of V_s−TiS_3 nanobelts after 5 and 10 cycles at 20 ℃ and other temperatures (Fig. 3F, S26, and S27). The activation energies were calculated from EIS based on the following equation:

$$i_o = A_o e^{\frac{-E_a}{RT}} \quad (1)$$

in which i_o is the exchange current density, A_o is a constant character, E_a represents the activation energy, R is the molar gas constant, and T is the temperature. The calculated activation energy of V_s−TiS_3 nanobelts after 10 cycles is 23.4 kJ mol^{-1}, which is smaller than that after 5 cycles (34.8 kJ mol^{-1}), verifying that a cathode activation process occurs during cycling (Fig. 3E). In contrast, activation energies for vacancy−free TiS_3 nanobelts are calculated to be 45.8 kJ mol^{-1} and 25.3 kJ mol^{-1} after 5 and 10 cycles, respectively. For non−(001) facet TiS_3, activation energies are calculated to be 54.0 kJ mol^{-1} and 29.6 kJ mol^{-1} after 5 and 10 cycles, respectively (Fig. S28−30). Overall, the electrochemical performance of V_s−TiS_3 is superior to that of other TMC−based cathodes, highlighting the advantages of S defects and exposed facets in V_s−TiS_3 cathodes (Fig. 3F).[3a, 9, 17b, 19] Further, the V_s−TiS_3 nanobelt cathode was employed in pouch cells to evaluate its practicability (Fig. S31). The tested pouch cell achieved an energy density of 220 Wh kg^{-1} with a capacity of 203 mAh g^{-1} after 30 cycles, with comparable performance to other TMC cathodes in MIBs (Table S4).[3a, 19c, 20a, 20b]

To investigate the energy storage mechanism during the discharge/charge process, ex−situ TEM images, XRD patterns, X−ray absorption near−edge structure (XANES) spectroscopy, and extended X−ray absorption fine structure (EXAFS) spectroscopy (Fig. 4 and 5) were employed. Ex−situ TEM images reveal that the nanobelt morphology of V_s−TiS_3 is maintained throughout the repeated Mg^{2+} insertion/extraction (Fig. 4A−F), indicative of the morphology's stability. The corresponding HRTEM images (Fig. 4G−L) show the structural evolution during the discharge/charge process. The specific lattice fringes are measured at 0.14 nm at 0.8 V, which is assigned to the (006) plane of TiS_3. When further discharged to 0.4 V, the characteristic plane [0.46 nm, $(\bar{1}01)$] for TiS_3 is still observed. At the end of discharge (0.01 V), the typical lattice fringe spacing of 0.31 nm is observed, (Fig. 4I) which is assigned to the (100) plane of TiS_2. These observations illustrate a stepwise process in which the V_s−TiS_3 nanobelts evolve during the insertion of Mg^{2+}, involving a hybrid of insertion and conversion storage mechanisms. Upon charging to 1.3 V, the typical lattice fringe spacing of 0.26 nm is observed for the (101) plane of TiS_2. Further charging to 1.6 V yields the appearance of characteristic lattice fringes of 0.36 nm associated with the $(\bar{1}02)$ plane of TiS_3, demonstrating the conversion of TiS_2 to TiS_3. At the full charge state of 2.0 V, the typical lattice fringe for TiS_2 persists, indicating an incomplete conversion reaction between TiS_2 and TiS_3. In addition, the above observations at different potential states are further corroborated with scanning transmission electron microscopy (STEM) and selected area electron diffraction (SAED) patterns (Fig. S32). Moreover, STEM images and corresponding elemental maps (Fig. 4M−R) obtained at differing discharge/charge states reveal homogenous distributions of elemental Mg, S, and Ti, corroborating uniform insertion and conversion throughout the nanobelt structure.

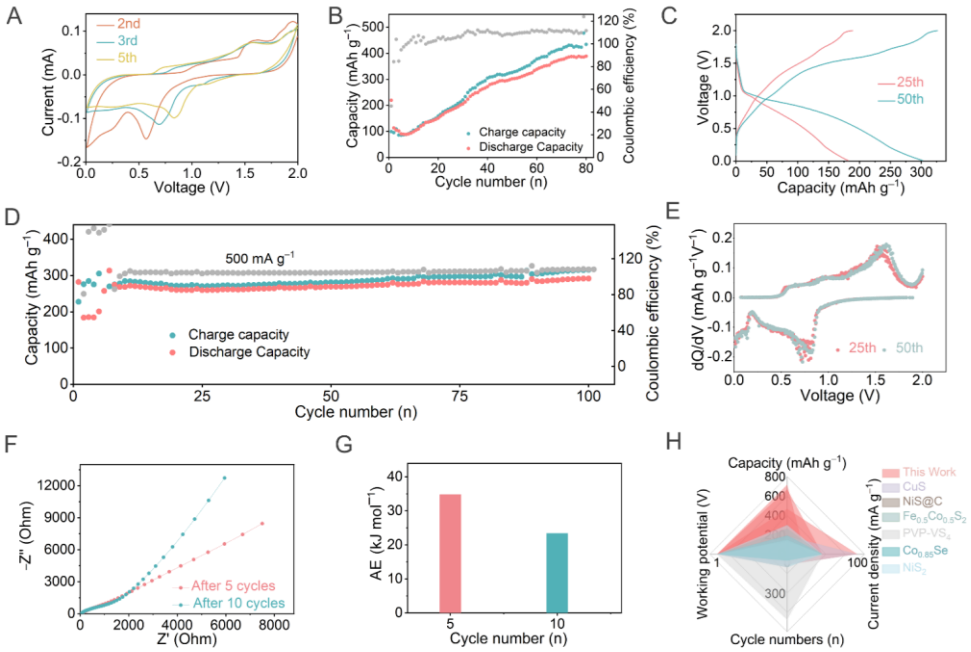

Fig. 3 Electrochemical performances of V_5−TiS_3 nanobelts cathodes. (A) CV curves at 0.2 mV s^{-1}, (B) cycling performance at 100 mA g^{-1}, (C) the corresponding charge−discharge profiles at 100 mA g^{-1}, (D) cycling performance at 500 mA g^{-1}, (E) the corresponding dQ/dV curves after 25th and 50th cycles. (F) EIS spectra after 5 and 10 cycles. (G) The activation energies after 5 cycles and after 10 cycles, (H) radar plot of electrochemical performances of TMC−based cathodes.

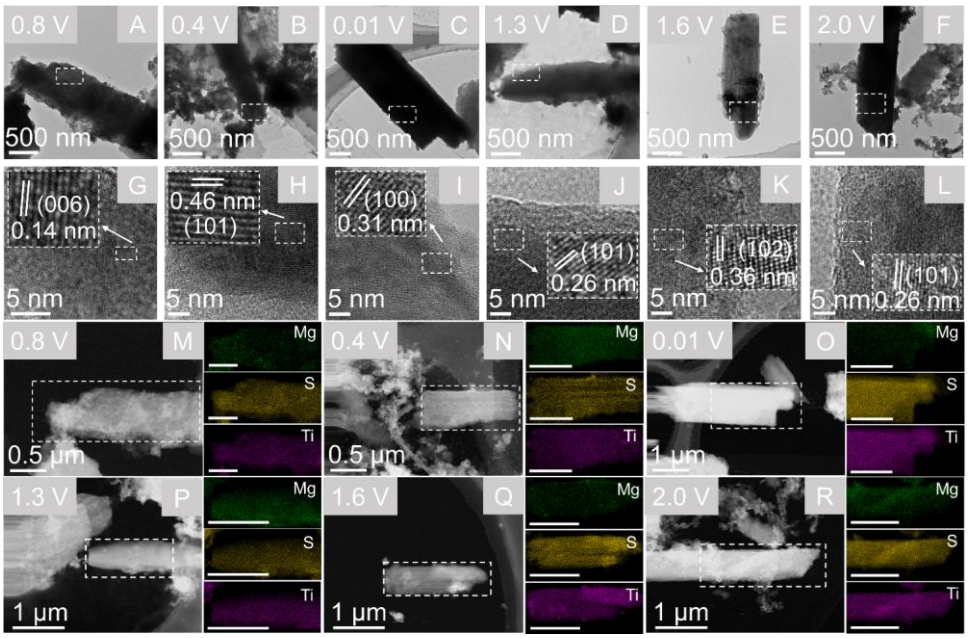

Fig. 4 Investigation of working principles: ex−situ TEM images and corresponding HRTEM images of V_S−TiS_3 nanobelts at different depths of discharge at (A, G) 0.8 V, (B, H) 0.4 V, (C, I) 0.01 V, (D, J) 1.3 V, (E, K) 1.6 V, (F, L) 2.0 V *vs.* Mg/Mg^{2+}, respectively. (M−R) The STEM images and corresponding EDS mapping images of Mg, S, and Ti elements collected at varied potential states (Scale bar: (M) 0.5 μm, (N) 0.5 μm, (O) 1 μm, (P) 1 μm, (Q) 1 μm, and (R) 1 μm).

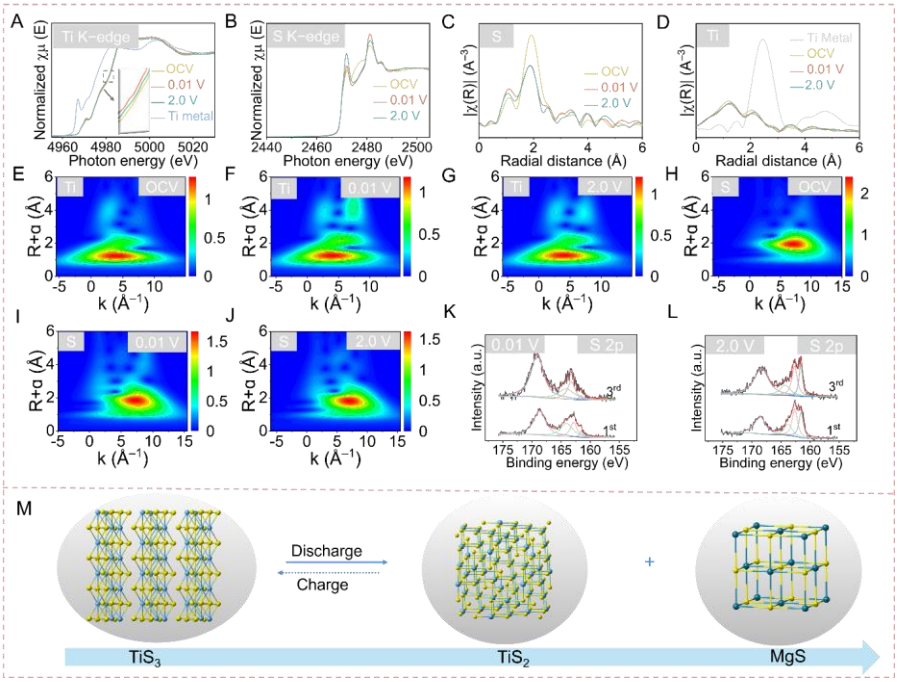

Fig. 5 Investigation of working principles in V_s–TiS_3 nanobelts cathodes: ex−situ (A) XANES spectra of Ti K−edge and (B) S K−edge, respectively. The corresponding Fourier transforms of k^3−weighted of (C) Ti K−edge EXAFS, and (D) S K−edge EXAFS at the discharge/charge states. (E−G) Wavelet transform 2D plots for Ti K−edge EXAFS, and (H−J) S K−edge EXAFS at different potential states. XPS spectra of S 2p collected from (K) discharged and (L) charged states. (M) Schematic illustration of irreversible electrochemical storage mechanism.

In the XANES spectra before cycling and after the discharge/charge process (Fig. 5A), the Ti K−edge spectrum shows a slight shift towards a lower photon energy after the insertion of Mg^{2+} (0.01 V), while the charge state (2.0 V) of the Ti K−edge XANES profile does not recover to its original position. This suggests that irreversible reactions occurred in the discharge/charge cycles, similar to observations made in lithium−ion batteries.[21] Moreover, the absence of a characteristic Ti peak in the pre−edge region reflects the absence of a conversion reaction from TiS_3 to Ti.

In the corresponding XANES spectra of the S K−edge (Fig. 5B), there are no significant shifts of photon energy relative to the measured elemental S powder and FeS (Fig. S33). To determine the storage mechanism, we performed EXAFS experiments (Fig. 5C, D). The Fourier−transformed (FT) curves of the S K−edge EXAFS spectra (Fig. 5C) show a characteristic peak at 1.86 Å, which is ascribed to S−S, in agreement with the peaks observed for S powder and FeS (Fig. S34). The intensity of S−S peak decreases dramatically with discharge to 0.01 V and does not recover to its initial intensity upon returning to the charged state (2.0 V). This reflects irreversible structural changes induced by the insertion/extraction process in V_s–TiS_3, as previously evidenced by TEM. Relative to the Ti−Ti bonds in Ti metal, the prominent peak observed at 2.05 Å in the FT curves of the Ti K−edge EXAFS spectra for V_s–TiS_3 is assigned to Ti−S. The peak intensity decreases upon discharging to 0.01 V (Fig. 5D) and similarly does not recover to its initial intensity upon charging back to 2.0 V, mirroring the trend of the S K−edge FT curves. The above trends are further illustrated in the corresponding wavelet transform 2D plots (Fig. 5E−G and S35), with the central position of S decreasing relative to its initial state at OCV (Fig. 5H) when discharged to 0.01 V (Fig. 5I), and partial recovery of the position at its fully charged state (Fig. 5J). The results point towards an incomplete recovery of the initial V_s–TiS_3 structure and suggest the presence of irreversible reactions during the discharging process.

Ex−situ XPS spectra were obtained at 0.01 V and 2.0 V after the 1st and 3rd cycles (Fig. 5K and L respectively). At 0.01 V, the binding energies at 164.0 eV and 163.2 eV of $(S_2)^{2-}$ are evident, while the binding energies at 163.2 eV and 161.5 eV are attributed to S^{2-} of S 2p, indicating an incomplete conversion reaction from TiS_3 to TiS_2. Furthermore, the intensity of the characteristic peak

of $(S_2)^{2-}$ at 164.0 eV after the 3rd cycle is lower than that after the 1st cycle, suggesting that the degree of conversion increases with subsequent cycles, further supporting the presence of an activation process (Fig. 5K). At 2.0 V, the characteristic peaks for S^{2-} and $(S_2)^{2-}$ remain, though the ratio of S^{2-} is markedly higher. This supports the hypothesis of an irreversible reaction during the discharge process as proposed above (Fig. 5L). The overall electrochemical process (Fig. 5M) can thus be summarized as follows:

$$TiS_3 + Mg^{2+} + 2e^- \rightarrow TiS_2 + MgS \quad (1)$$

$$TiS_2 + xMg^{2+} + 2xe^- \leftrightarrow Mg_xTiS_2 \quad (2)$$

XPS depth profiling of V_s−TiS_3 after 30 and 75 cycles with etching times of 0, 1, 4, and 8 min was conducted to confirm the presence of sulfur vacancies in the cycling process (Fig. S36 B−C). For comparison, XPS depth profiling of TiS_3 after 30 cycles with the same etching times was also collected (Fig. S36 A). Due to significant signal−to−noise ratio, deconvolution of the Ti 2p spectra was not conducted for all the samples without etching. In Ti 2p of TiS_3 after 30 cycles, the fitted pairs of peaks at 457.1 eV and 463.2 eV, alongside 459.0 eV and 464.9 eV, are associated with Ti−S bonding and Ti−O bonding respectively.[12] For V_s−TiS_3 after 30 cycles, the fitted peaks of Ti 2p were shifted towards lower binding energies relative to TiS_3, at 456.3 eV and 462.3 eV, as well as 458.5 eV and 464.3 eV, which supports the presence of sulfur vacancies.[14] Moreover, the fitted peaks of Ti 2p in V_s−TiS_3 after 75 cycles are similar to V_s−TiS_3 after 30 cycles, indicating that the sulfur vacancies are maintained during long−term cycling. The fitted peaks Ti 2p across etching times in each sample are consistent, demonstrating that the presence of sulfur vacancies extends throughout the bulk material (Fig. S36).

To account for the notable electrochemical performance of the V_s−TiS_3 nanobelts, we used MLFF−MD simulations to explore diffusion and the interactions of interfaces between Mg and TiS_3. From the interface modes between Mg(001) plane and TiS_3(001) plane after differing times in the simulated process, we observe that the interface is very active and that Mg atoms can diffuse into the structures of TiS_3 after a few picoseconds (Fig. 6A). At 100 ps, Mg atoms around the interface almost completely diffuse into structures of TiS_3, indicating that the (001) plane of TiS_3 is favorable to facilitate reactions with Mg. This is further supported by the corresponding pair distribution function data and running coordination numbers of Mg−S and Ti−S (Fig. S37, S38), showing rapid variations observed during the ongoing simulation process. To further highlight the advantages of the TiS_3(001) exposed facets, we also fabricated the interface modes between Mg(001) and TiS_3(010), as well as Mg(001) and TiS_3(100) (Fig. 6B and C respectively). For both facets, slower diffusion of Mg atoms into TiS_3 structures is observed, indicating that the exposed TiS_3(001) facets allow the fastest insertion of Mg^{2+} compared to the (100) and (010) facets. The corresponding pair distribution function data and running coordination numbers of Mg−S and Ti−S in the interfaces of TiS_3(010) and TiS_3(100) evolve at a slower rate (Fig. S39−S42), validating the results of the simulated modes.

To further understand the electrochemical processes and account for the increasing capacity in the initial cycles, we quantitatively analyzed anion distributions on both the cathode and anode after 3, 5, and 20 cycles with time−of−flight secondary ion mass spectrometry (TOF−SIMS) (Fig. 6D, 6E, S43−47). The depth profiles reveal that the distribution of negative ions (e.g., TiS^-, TiS_2^-, TiS_3^-, S^-, S_2^-, S_4^-, MgS^-, and MgS_4^-) on the surface of the cathode differs slightly between the 3rd and 5th cycles (Fig. S44A−D). In contrast, the intensity ratios of anions (MgS^-/TiS^-, MgS^-/TiS_2^-) on the surface of the cathode substantially increased after 20 cycles, indicating that the degree of conversion reaction is enhanced, and accounting for the enhanced capacity during cycling (Fig. S47). Additionally, the intensity ratios of secondary anions profile on the surface of the anode (MgS^-/S^-, S_2^-/S^-) after 20 cycles are similar to those after 3 cycles and 5 cycles, reflecting restrained shuttling effects during cycling.

We also investigated the distribution of secondary cations (Mg^+, Ti^+) on both electrodes with TOF−SIMS (Fig. S48, S49). The lower amount of Mg^+ left in the cathode after the 5th cycle relative to the 3rd cycle supports our above hypothesis that an activation process occurs within the initial cycles. The cryo−STEM image and corresponding EDS images (Fig. 6F−H) obtained from the Mg anode confirm the presence of MgS_x, indicative that the shuttling effects still occur to a degree during the electrochemical processes in V_s−TiS_3 nanobelts, which remains a problem to be mitigated further. In our later work, we will retard the shuttle effects from the optimization of electrolytes, via changing the electron transfer pathway in magnesium polysulfides.

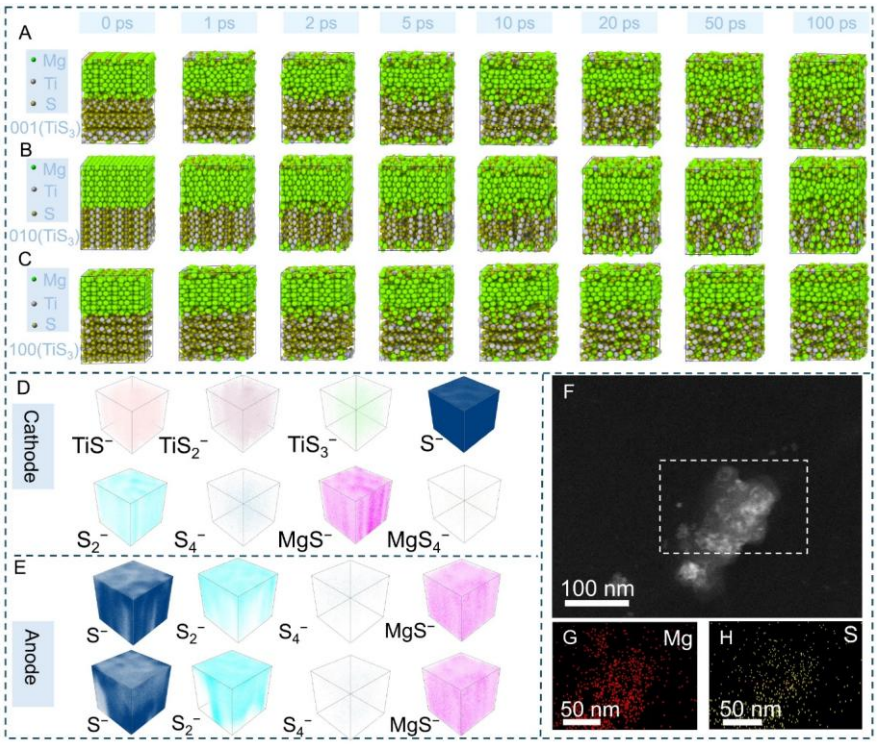

Fig. 6 MLFF−MD simulations and investigations in electrochemical process: Interface modes of (A) TiS_3(001)−Mg(001), (B) TiS_3(010)−Mg(001), and (C) TiS_3(100)−Mg(001) before MLFF−MD simulation and after different times of simulation. (D) The reconstructed 3D spatial fragment distributions of anions (TiS^-, TiS_2^-, TiS_3^-, S^-, S_2^-, S_4^-, MgS^-, and MgS_4^-) on the side of cathode after 5 cycles, (E) and the anions on the side of anode after 3 and 5 cycles, respectively. (F−H) Cryogenic STEM images of MgS_x collected from the Mg anode and corresponding mapping images of Mg and S elements, respectively.

Conclusion

We developed defective V_s−TiS_3 nanobelts with exposed (001) facets via rapid quenching and investigated their use as cathodes for MIBs. We also proposed and discussed a hybrid storage mechanism in which the electrode first undergoes conversion and subsequently reacts via insertion. More importantly, the intermediates of defective TiS_2 were found to have a strong adsorption effect on MgS_x, accounting for the remarkable electrochemical storage performance observed. We found that the exposed (001) facets and defects in V_s−TiS_3 nanobelts provide multichannel transport for Mg^{2+} to enhance the electrochemical kinetics through XAS spectra, cryo−TEM images, TOF−SIMS, DFT calculations, and MLFF−MD simulations. This results in the cathode delivering a high capacity of 717.3 mAh g^{-1} at 25 mA g^{-1}. When evaluated at the level of pouch cells, we achieved a substantially high energy density of 220 Wh kg^{-1}, highlighting the potential of defective V_s−TiS_3 nanobelts for practical applicability in MIBs. Notably, the versatility of the electrodes was also explored in lithium−ion batteries, sodium−ion batteries, and aluminum−ion batteries, which can provide some new insights for designing advanced electrodes for high energy density batteries.

Acknowledgements

Z. W. Seh acknowledges support by the Singapore National Research Foundation (NRF Investigatorship NRF-NRFI09-0002) and the Agency for Science, Technology and Research (MTC Programmatic Fund M23L9b0052). Q. Yan acknowledges Indonesia-NTU Singapore Institute of Research for Sustainability and Innovation (INSPIRASI) under contract no. 6635/E3/KL.02.02/2023, and Singapore NRF Singapore-China

flagship program under grant no. 023740-00001. We acknowledge the National Supercomputing Center (NSCC) Singapore and Agency for Science, Technology and Research (A*STAR) Computational Resource Centre (A*CRC) of Singapore for the use of its high-performance computing facilities.

Keywords: Hybrid storage mechanism • Transition metal polyanions • Cathode • Rechargeable Magnesium Batteries

References:

[1] a) A. Y. S. Eng, C. B. Soni, Y. Lum, E. Khoo, Z. Yao, S. Vineeth, V. Kumar, J. Lu, C. S. Johnson, C. Wolverton, Sci. Adv. 2022, 8, eabm2422; b) Z. Yao, Y. Lum, A. Johnston, L. M. Mejia-Mendoza, X. Zhou, Y. Wen, A. Aspuru-Guzik, E. H. Sargent, Z. W. Seh, Nat. Rev. Mater. 2023, 8, 202-215; c) J. Wang, N. Luo, J. Wu, S. Huang, L. Yu, M. Wei, J. Mater. Chem. A 2019, 7, 3691-3696; d) K. Liu, Y. Liu, D. Lin, A. Pei, Y. Cui, Sci. Adv. 2018, 4, eaas9820.

[2] a) J. Wang, J. Okabe, K. Urita, I. Moriguchi, M. Wei, J. Electroanal. Chem. 2020, 874; b) Y. Liang, Y. Yao, Nat. Rev. Mater. 2022, 8, 109-122; c) J. Wang, J. Huang, S. Huang, Y. Komine, H. Notohara, K. Urita, I. Moriguchi, M. Wei, Chem. Eng. J. 2022, 429, 132424; d) J. Wang, J. Okabe, Y. Komine, H. Notohara, K. Urita, I. Moriguchi, M. Wei, Sci. China Technol. Sci. 2022, 65, 1859-1866.

[3] a) J. Wang, T. Ghosh, Z. Ju, M.-F. Ng, G. Wu, G. Yang, X. Zhang, L. Zhang, A. D. Handoko, S. Kumar, Matter 2024, 7, 1833-1847; b) J. Wang, Z. W. Seh, Acc. Mater. Res. 2024, 5(11), 1329–1339.

[4] a) Y. Liang, H. Dong, D. Aurbach, Y. Yao, Nat. Energy 2020, 5, 646-656; b) H. Dong, O. Tutusaus, Y. Liang, Y. Zhang, Z. Lebens-Higgins, W. Yang, R. Mohtadi, Y. Yao, Nat. Energy 2020, 5, 1043-1050.

[5] a) C. Li, L. Lin, W. Wu, X. Sun, Small Methods 2022, 6, e2200363; b) K. Shimokawa, T. Atsumi, N. L. Okamoto, T. Kawaguchi, S. Imashuku, K. Wagatsuma, M. Nakayama, K. Kanamura, T. Ichitsubo, Adv. Mater. 2021, 33, e2007539; c) Y. Yang, J. Zhou, L. Wang, Z. Jiao, M. Xiao, Q.-a. Huang, M. Liu, Q. Shao, X. Sun, J. Zhang, Nano Energy 2022, 99, 107424.

[6] D. Chen, D. Tao, X. Ren, F. Wen, T. Li, Z. Chen, Y. Cao, F. Xu, ACS Nano 2022, 16, 20510-20520.

[7] a) W. Kaveevivitchai, A. J. Jacobson, Chem. Mater. 2016, 28, 4593-4601; b) I. D. Johnson, B. J. Ingram, J. Cabana, ACS Energy Lett. 2021, 6, 1892-1900; c) L. Ma, H. Cui, S. Chen, X. Li, B. Dong, C. Zhi, Nano Energy 2021, 81, 105632.

[8] Z. Li, J. Häcker, M. Fichtner, Z. Zhao-Karger, Adv. Energy Mater. 2023, 13, 2300682.

[9] J. Wang, G. Yang, T. Ghosh, Y. Bai, C. Y. J. Lim, L. Zhang, D. H. L. Seng, W. P. Goh, Z. Xing, Z. Liu, Z. W. Seh, Nano Energy 2024, 119, 109082.

[10] A. Roy, M. Sotoudeh, S. Dinda, Y. Tang, C. Kubel, A. Gross, Z. Zhao-Karger, M. Fichtner, Z. Li, Nat. Commun. 2024, 15, 492.

[11] J. Park, S. J. Kim, K. Lim, J. Cho, K. Kang, ACS Energy Lett. 2022, 7, 3718-3726.

[12] C. Liu, C. Wu, X. Y. Tan, Y. Tao, Y. Zhang, D. Li, J. Yang, Q. Yan, Y. Chen, Nat. Commun. 2023, 14, 5597.

[13] a)Q. Fan, X. Lv, J. Lu, W. Guo, Y. Fu, Proc. Natl. Acad. Sci. U. S. A. 2023, 120, e2219395120; bM. E. Fleet, S. L. Harmer, X. Liu, H. W. Nesbitt, Surf. Sci. 2005, 584, 133-145.

[14] J. Wang, J. Huang, S. Huang, H. Notohara, K. Urita, I. Moriguchi, M. Wei, ACS Sustain. Chem. & Eng. 2020, 8, 9519-9525.

[15] K. K. Mishra, T. R. Ravindran, J. O. Island, E. Flores, J. R. Ares, C. Sanchez, I. J. Ferrer, H. S. J. van der Zant, A. Pawbake, R. Kanawade, A. Castellanos-Gomez, D. J. Late, ACS Appl. Nano Mater. 2020, 3, 8794-8802.

[16] K. Wu, E. Torun, H. Sahin, B. Chen, X. Fan, A. Pant, D. Parsons Wright, T. Aoki, F. M. Peeters, E. Soignard, S. Tongay, Nat. Commun. 2016, 7, 12952.

[17] a) S. Zhuo, G. Huang, R. Sougrat, J. Guo, N. Wei, L. Shi, R. Li, H. Liang, Y. Shi, Q. Zhang, P. Wang, H. N. Alshareef, ACS Nano 2022, 16, 3955-3964; b) J. Wang, A. D. Handoko, Y. Bai, G. Yang, Y. Li, Z. Xing, M. F. Ng, Z. W. Seh, Nano Lett. 2022, 22, 10184-10191.

[18] a) G. Alvarez Ferrero, G. Åvall, K. A. Mazzio, Y. Son, K. Janßen, S. Risse, P. Adelhelm, Adv. Energy Mater. 2022, 12, 2202377; b) S. Zhuo, G. Huang, Y. Lei, W. Wang, Z. Liu, X. Xu, J. Yin, H. N. Alshareef, Small Methods 2020, 4, 2000439; c) G. Sun, Z. Wei, N. Chen, G. Chen, C. Wang, F. Du, Chem. Eng. J. 2020, 388, 124305; d) Z. Hu, Z. Tai, Q. Liu, S. W. Wang, H. Jin, S. Wang, W. Lai, M. Chen, L. Li, L. Chen, Z. Tao, S. L. Chou, Adv. Energy Mater. 2019, 9, 1801230; e) P. Hu, B. Wang, D. Xiao, K. Aifantis, Nano Energy 2019, 63, 103820.

[19] a) Y. Fei, Y. Man, J. Sun, Y. Du, B. Chen, J. Bao, X. Zhou, Small 2023, 19, e2301954; b) G. Zhu, G. Xia, H. Pan, X. Yu, Adv. Sci. (Weinh) 2022, 9, e2106107; c) H. Xu, Y. Li, D. Zhu, Z. Li, F. Sun, W. Zhu, Y. Chen, J. Zhang, L. Ren, S. Zhang, J. Zou, R. M. Laine, Adv. Energy Mater. 2022, 12, 2202377; d) D. Chen, F. Du, S.-a. Cao, T. Li, F. Xu, Chem. Eng. J. 2022, 428, 2201608.

[20] a) Y. Zhang, J. M. Cao, Z. Yuan, H. Xu, D. Li, Y. Li, W. Han, L. Wang, Small 2022, 18, e2202313; b) D. Lu, H. Liu, T. Huang, Z. Xu, L. Ma, P. Yang, P. Qiang, F. Zhang, D. Wu, J. Mater. Chem. A 2018, 6, 17297-17302.

[21] a) S. Saha, G. Assat, M. T. Sougrati, D. Foix, H. Li, J. Vergnet, S. Turi, Y. Ha, W. Yang, J. Cabana, G. Rousse, A. M. Abakumov, J.-M. Tarascon, Nat. Energy 2019, 4, 977-987; b) K. Kumar, N. Sunariwal, J. Louis, B. T. Leube, I. Roy, G. E. Sterbinsky, J. M. Tarascon, J. Cabana, Adv. Funct. Mater. 2024, 34, 2408060.

设置了格式: 英语(美国)

Entry for the Table of Contents

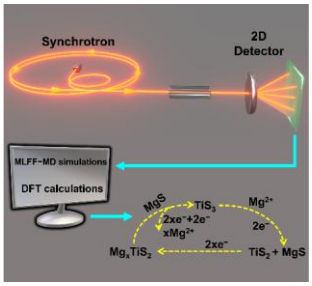

The cathode was investigated in MIBs with synchrotron X−ray absorption spectra, demonstrating a new hybrid energy storage mechanism involving both insertion and conversion reactions.